



# A phase transformation-free redox couple mediated electrocatalytic oxygen evolution reaction

Yu Du<sup>a,1</sup>, Depei Liu<sup>a,b,1</sup>, Taozhu Li<sup>a</sup>, Yuandong Yan<sup>a</sup>, Yan Liang<sup>c</sup>, Shicheng Yan<sup>a,\*</sup>, Zhigang Zou<sup>a,b</sup>

<sup>a</sup> Eco-materials and Renewable Energy Research Center (ERERC), Collaborative Innovation Center of Advanced Microstructures, College of Engineering and Applied Sciences, Nanjing University, No. 22 Hankou Road, Nanjing, Jiangsu 210093, PR China

<sup>b</sup> Jiangsu Key Laboratory for Nano Technology, National Laboratory of Solid State Microstructures, School of Physics, Nanjing University, No. 22 Hankou Road, Nanjing, Jiangsu 210093, PR China

<sup>c</sup> Key Laboratory of Solar Energy Science and Technology in Jiangsu Province, Southeast University, No. 2 Si Pai Lou, Nanjing, Jiangsu 210096, PR China

## ARTICLE INFO

### Keywords:

Iron nickel hydroxide

Ni<sup>2+</sup>/Ni<sup>3+</sup> redox

CeO<sub>2-x</sub> decoration

Oxygen evolution reaction

## ABSTRACT

NiFe layered double hydroxide (NiFe-LDH), as a promising non-noble catalyst for oxygen evolution reaction (OER), suffers from the high OER barriers during Ni<sub>x</sub>Fe<sub>1-x</sub>(OH)<sub>2</sub>/Ni<sub>x</sub>Fe<sub>1-x</sub>OOH interconversion. To solve this problem, we highly dispersed the 2–3 nm CeO<sub>2-x</sub> particles on single-layered NiFe-LDH to form CeO<sub>2-x</sub>/NiFe-LDH heterostructure by a one-step co-precipitation method. CeO<sub>2-x</sub>, as an electron acceptor, can extract electrons from Ni sites of NiFe-LDH via Ni-O-Ce electron exchange effect, thus achieving direct Ni<sup>2+</sup>/Ni<sup>3+</sup> electron transfer with no need of Ni<sub>x</sub>Fe<sub>1-x</sub>(OH)<sub>2</sub>/Ni<sub>x</sub>Fe<sub>1-x</sub>OOH phase transformation. As a result of efficient electron transfer by strong interface interactions between CeO<sub>2-x</sub> and NiFe-LDH, the CeO<sub>2-x</sub>/NiFe-LDH exhibits excellent OER performance with a low OER overpotential of 216 mV at 10 mA cm<sup>-2</sup> and a Tafel slope of 74.1 mV dec<sup>-1</sup>. Our work provides a new strategy to improve the OER performances of NiFe-based materials.

## 1. Introduction

Oxygen evolution reaction (OER), involving a four-step proton coupling electron transfer process, is a crucially anodic reaction of energy storage and conversion technologies, such as water splitting [1,2], CO<sub>2</sub> reduction reaction [3,4] and rechargeable metal-air batteries [5,6]. Whereas, its sluggish kinetics seriously limits energy conversion efficiency. Currently, commercial noble metal catalysts (IrO<sub>2</sub>, Ir/C, RuO<sub>2</sub>, Ru/C, etc.) with high activity suffer from high cost and low abundance [7]. To conquer these problems, developing efficient earth-abundant metal-based OER electrocatalysts has attracted great attentions [8]. NiFe layered double hydroxide (NiFe-LDH) is regarded as the most promising candidates due to unique structure and simple preparation [9–11].

However, the intrinsic activity of NiFe-LDH is limited by the high energy barrier for the deprotonation of Ni<sub>x</sub>Fe<sub>1-x</sub>(OH)<sub>2</sub>/Ni<sub>x</sub>Fe<sub>1-x</sub>OOH phase transformation during OER process (Ni<sub>x</sub>Fe<sub>1-x</sub>(OH)<sub>2</sub> → Ni<sub>x</sub>Fe<sub>1-x</sub>OOH + H<sup>+</sup> + e<sup>-</sup>) [12,13]. Given this challenge, many strategies, such as defect introduction [14–16], element doping [17–20], layer

exfoliation [21–24], and heterostructure construction [25–28], have been developed to tune the local electron configurations of Ni or/and Fe sites to accelerate the electron transfer kinetics of Ni<sup>2+</sup>/Ni<sup>3+</sup> via Ni<sub>x</sub>Fe<sub>1-x</sub>(OH)<sub>2</sub>/Ni<sub>x</sub>Fe<sub>1-x</sub>OOH interconversion. Obviously, the electron transfer barriers can be further reduced if we can create a Ni<sup>2+</sup>/Ni<sup>3+</sup> electron transfer with no need of deprotonation of Ni<sub>x</sub>Fe<sub>1-x</sub>(OH)<sub>2</sub>/Ni<sub>x</sub>Fe<sub>1-x</sub>OOH phase transformation. Indeed, the deprotonation of Ni<sub>x</sub>Fe<sub>1-x</sub>(OH)<sub>2</sub> to form Ni<sub>x</sub>Fe<sub>1-x</sub>OOH results from the requirement of valency balance during Ni<sup>2+</sup>/Ni<sup>3+</sup> oxidation. Thus, we hope using a redox to replace the protons of -OH groups on NiFe-LDH to keep charge balance, achieving a Ni<sup>2+</sup>/Ni<sup>3+</sup> oxidation without Ni<sub>x</sub>Fe<sub>1-x</sub>(OH)<sub>2</sub>/Ni<sub>x</sub>Fe<sub>1-x</sub>OOH interconversion.

In this work, we found that decorating CeO<sub>2</sub> as an electron transfer mediator via Ce<sup>3+</sup>/Ce<sup>4+</sup> redox can achieve directly Ni<sup>2+</sup>/Ni<sup>3+</sup> redox in NiFe-LDH with no need of Ni<sub>x</sub>Fe<sub>1-x</sub>(OH)<sub>2</sub>/Ni<sub>x</sub>Fe<sub>1-x</sub>OOH transformation during OER process [29–33]. The heterostructure with tight junction interface between ultrasmall CeO<sub>2-x</sub> nanoparticles and single-layered NiFe-LDH (CeO<sub>2-x</sub>/NiFe-LDH) was synthesized by one-step co-precipitating Ni<sup>2+</sup>, Fe<sup>3+</sup> and Ce<sup>4+</sup> in formamide-containing basic solution.

\* Corresponding author.

E-mail address: [yscfei@nju.edu.cn](mailto:yscfei@nju.edu.cn) (S. Yan).

<sup>1</sup> These authors contributed equally to this work.

Experimental results demonstrated that the  $\text{Ce}^{4+}$  as strong electron acceptor extracted electrons from Ni sites by the exchange effect of Ni-O-Ce, which leads the  $\text{Ni}^{2+}/\text{Ni}^{3+}$  oxidation without phase change, sharply decreasing the energy barrier of  $\text{Ni}^{2+}/\text{Ni}^{3+}$  redox. As a result,  $\text{CeO}_{2-x}/\text{NiFe-LDH}$  exhibits excellent OER performance with a low Tafel slope of  $74.1 \text{ mV dec}^{-1}$  and overpotential of 216 mV at  $10 \text{ mA cm}^{-2}$ . This work provides a new insight into developing of high-activity redox couple mediated OER catalysts.

## 2. Experimental section

### 2.1. Chemicals

All chemicals were analytical reagents and used as obtained without further purification. Nickel nitrate hexahydrate ( $\text{Ni}(\text{NO}_3)_2 \cdot 6\text{H}_2\text{O}$ ), iron nitrate nonahydrate ( $\text{Fe}(\text{NO}_3)_3 \cdot 9\text{H}_2\text{O}$ ), Sodium hydroxide (NaOH), potassium hydroxide (KOH), and ethanol were purchased from Shanghai Chemical Reagent Co., Ltd (China). Formamide was purchased from China National Medicines Co., Ltd (China). Ammonium ceric nitrate ( $\text{Ce}(\text{NH}_4)_2(\text{NO}_3)_6$ ) was purchased from Shanghai Rhawn Reagent Co., Ltd (China). Deionized water was used in all experiments.

### 2.2. Preparation of $\gamma\text{-CeO}_{2-x}/\text{NiFe-LDH}$

0.75 mmol  $\text{Ni}(\text{NO}_3)_2 \cdot 6\text{H}_2\text{O}$ , 0.25 mmol  $\text{Fe}(\text{NO}_3)_3 \cdot 9\text{H}_2\text{O}$  and  $\gamma \mu\text{mol}$   $\text{Ce}(\text{NH}_4)_2(\text{NO}_3)_6$  ( $\gamma = 0, 50, 150$  or  $300$ ) were dissolved in 20 mL deionized water to form a clear aqueous solution at room temperature. Subsequently, the solution, together with 0.25 M NaOH, was added dropwise to 20 mL, 23 vol% formamide aqueous solution under magnetic stirring at  $80^\circ\text{C}$ . Moderate amount of 0.25 M NaOH was added to maintain a pH of  $\sim 10$ . The reaction was completed within 10 min. The  $\text{CeO}_{2-x}$  decorated single-layered NiFe LDHs with different amount of  $\text{CeO}_{2-x}$  was collected by 8000 rpm centrifugation of 10 min, and then washed by at least three centrifugation/redispersion cycles. The as-prepared samples were kept in the gel state for subsequent use. The  $\text{CeO}_2$  was prepared as the comparison sample by the same method except using 1 mmol  $\text{Ce}(\text{NH}_4)_2(\text{NO}_3)_6$  to replace  $\text{Ni}(\text{NO}_3)_2 \cdot 6\text{H}_2\text{O}$  and  $\text{Fe}(\text{NO}_3)_3 \cdot 9\text{H}_2\text{O}$ .

### 2.3. Characterizations

The crystal structures of prepared samples were characterized by X-ray diffraction (XRD, Rigaku Ultima III, Japan with  $\text{Cu K}\alpha$  radiation) at 40 kV and 40 mA from  $5^\circ$  to  $70^\circ$  with a scanning speed of  $2^\circ \text{ min}^{-1}$ . X-ray photoelectron spectroscopy (XPS, PHI5000 Versa Probe, ULVAC-PHI, Japan) for composition and chemical states with monochromatized Al  $\text{K}\alpha$  excitation (The binding energies were corrected by normalizing the C1s spectrum at 284.6 eV, and a Shirley background was used for peak fitting), transmission electron microscope (TEM), FEI Talos F200s equipped with scanning TEM (STEM) for morphology and crystal lattice image, the energy dispersive spectroscopy (EDS) for composition analysis, and the atomic resolution high angle annular dark field (HAADF) images, atomic force microscope (AFM, Asylum Research, MFP-3D-SA, USA) for thickness of nanosheets.

In Ce 3d XPS spectra, The Ce  $3d_{5/2}$  and  $3d_{3/2}$  doublets are usually denoted as u and v, respectively, including four pairs of the spin-orbital doublet peaks ( $3d_{5/2}$  and  $3d_{3/2}$ ):  $v/u$ ,  $v'/u'$ ,  $v''/u''$ ,  $v'''/u'''$  [34–36]. The  $v/u$ ,  $v'/u'$ , and  $v''/u''$  peaks refer to the characteristic  $\text{Ce}^{4+}$  3d final states, and  $v'/u'$  refer to  $\text{Ce}^{3+}$  3d final states. The content of  $\text{Ce}^{3+}$  species can be estimated using relative areas of  $v'/u'$  peaks according to the equation of  $[\text{Ce}^{3+}] = \frac{S_{v'} + S_{u'}}{\sum (S_{v'} + S_{u'})}$  [34,36], where S is the relative area corresponding to peak  $v'$  and  $u'$ .

### 2.4. Electrochemical tests

To prepare the catalyst ink, 5 mg of catalyst was dispersed in 940  $\mu\text{L}$  ethanol by sonication for 20 min and then another ultrasonication after adding 60  $\mu\text{L}$  Nafion (0.25 wt%, DuPont). Next, 25  $\mu\text{L}$  of ink was dropwise loaded on the carbon paper ( $0.5 \text{ cm} \times 1 \text{ cm}$ ). After drying at ambient conditions, the catalytic working electrode could be used for the electrochemical study.

The OER electrocatalytic performance was evaluated on a CHI 660e electrochemical workstation (CH Instruments, Inc., Shanghai) using a standard three-electrode system. The geometric surface area of catalyst loaded on the carbon paper is  $0.5 \text{ cm}^2$ , and the catalyst loading amount can be calculated as  $0.25 \text{ mg cm}^{-2}$ . Briefly, the above modified carbon paper electrode as the working electrode, meanwhile an Ag/AgCl (Sat.) electrode and a Pt plate were used as reference and counter electrode, respectively. All potentials in this study were given versus reversible hydrogen electrode (RHE) ( $E_{\text{RHE}} = E_{\text{Ag/AgCl}} + 0.0591 \cdot \text{pH} + 0.197$ ). The OER overpotential ( $\eta$ ) was calculated according to the  $\eta = E_{\text{RHE}} - 1.23 \text{ V}$ . Before testing, the working electrodes were stabilized after 50 cyclic voltammetry (CV) cycles. Linear sweep voltammetry (LSV) and CV curves were tested in 1.0 M KOH solution from 0 to 0.6 V (vs. Ag/AgCl) at a scan rate of  $5 \text{ mV s}^{-1}$ . The polarization curves were iR-corrected with respect to the ohmic resistance of solution. Electrochemical surface area (ECSA) is calculated by measuring double-layer capacitance ( $C_{\text{dl}}$ ) values by CV method in the non-Faradaic region from 1  $\sim$  1.2 V vs. RHE at the scan rate range of 20, 60, 100, 140, and  $180 \text{ mV s}^{-1}$ . ECSA can be calculated by equation  $\text{ECSA} = C_{\text{dl}}/C_s$ , where  $C_s$  is the specific capacitance of the sample which is usually  $0.040 \text{ mF cm}^{-2}$  in the alkaline solution. The ECSA-normalized current density is calculated by equation:  $j_{\text{ECSA}} = j / \text{ECSA}$ . To evaluate the stability of as-prepared catalysts, the chronopotentiometry was used at the current density of  $10 \text{ mA cm}^{-2}$  to get v-t curves. Electrochemical impedance spectroscopy (EIS) was tested in 1.0 M KOH solution by applying an AC voltage of 10 mV amplitude at the potential of 0.51 V (vs. Ag/AgCl) with frequency from 100 kHz to 0.1 Hz.

## 3. Results and discussion

### 3.1. Structural characterization of $\text{CeO}_{2-x}/\text{NiFe-LDH}$

In order to get the strong chemical connection between  $\text{CeO}_{2-x}$  and NiFe-LDH, as shown in Fig. 1a,  $\text{Ni}^{2+}$ ,  $\text{Fe}^{3+}$ , and  $\text{Ce}^{4+}$  ions were co-precipitated in formamide-containing basic solution ( $\text{pH} = 10$ ) to get the nanostructure by in-situ dispersing ultrasmall  $\text{CeO}_{2-x}$  nanoparticles on single-layered NiFe-LDH ( $\text{CeO}_{2-x}/\text{NiFe-LDH}$ ). Here, considering the ultrasmall size ( $< 5 \text{ nm}$ ) of cerium dioxide nanoparticles result in formation of abundant oxygen vacancies [35], they are denoted as  $\text{CeO}_{2-x}$  ( $0 < x < 0.5$ ). For comparison, the single-layered NiFe-LDH and  $\text{CeO}_2$  were synthesized by the same method using corresponding metal precursor solution. Formamide is strong polar molecules, easily adsorbing on the positively charged NiFe-LDH layers. The adsorbed formamide and anions create steric hindrance to weaken the Coulombic interactions of different NiFe-LDH layers, thus suppressing layers stacking along the z-axis.

The atomic force microscopy (AFM) observations indicated that both NiFe-LDH (Fig. 1b and c) and  $\text{CeO}_{2-x}/\text{NiFe-LDH}$  (Fig. 1e and f) are the nanosheets with a thickness of 0.7–0.8 nm, suggesting formation of a single-layer NiFe-LDH ( $\sim 0.8 \text{ nm}$ ) [37]. A clear Tyndall effect of their aqueous suspensions was a result of the small size of NiFe LDH nanosheets with high hydrophilicity (Fig. 1d and g).

The ultrathin NiFe-LDH and  $\text{CeO}_{2-x}/\text{NiFe-LDH}$  nanosheets were further confirmed by transmission electron microscope (TEM) image (Fig. 2). The high-resolution TEM (HRTEM) lattice fringes with spacings of 0.26 nm are indexed to the (012) facets of NiFe-LDH nanosheets (Fig. 2a and b). In contrast, the TEM image of  $\text{CeO}_{2-x}/\text{NiFe-LDH}$  (Fig. 2c) shows that the  $\text{CeO}_2$  nanoparticles with the size of about

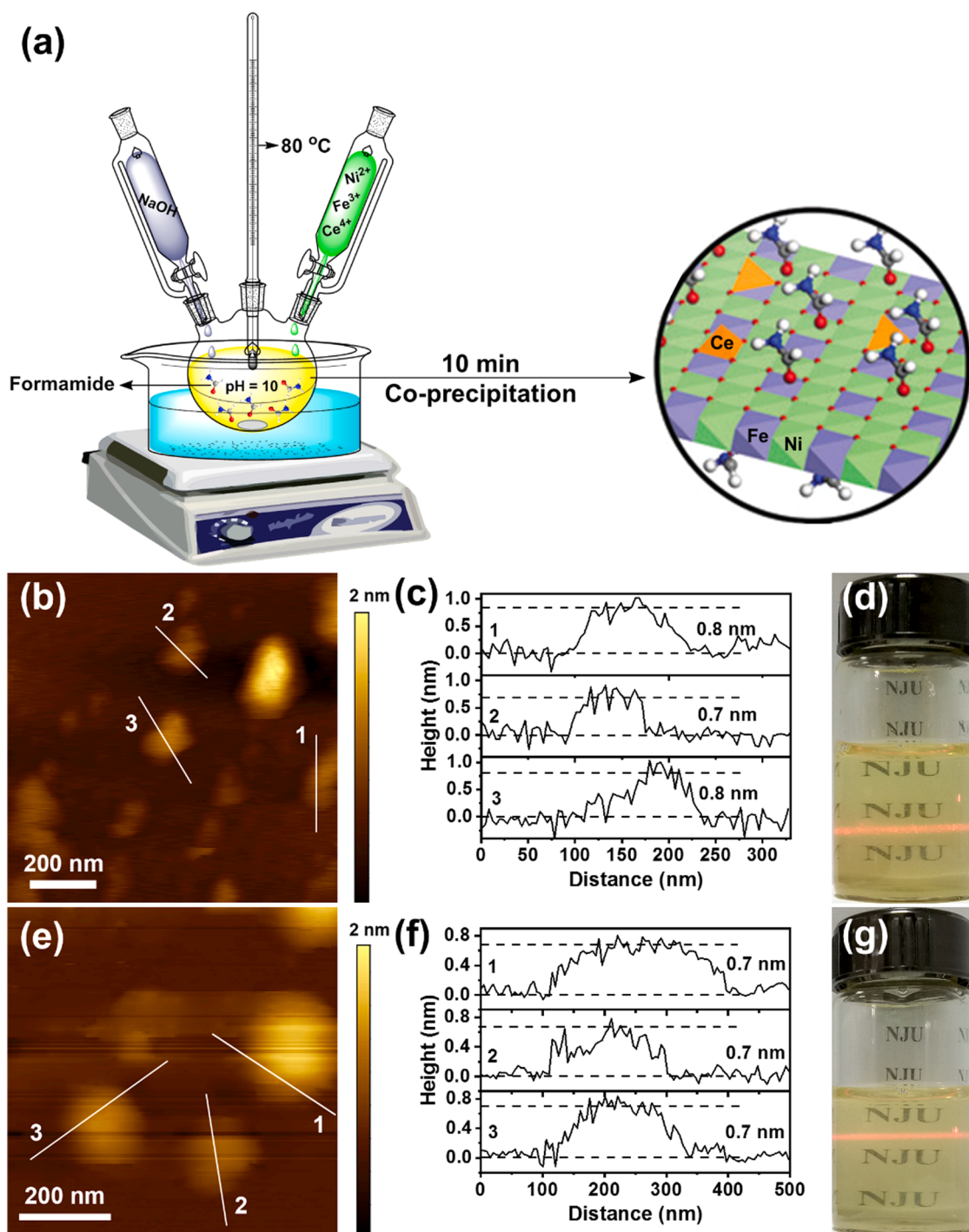


**Fig. 1.** (a) A schematic diagram of the preparation process for  $\text{CeO}_{2-x}/\text{NiFe-LDH}$ . AFM images, height profiles and Tyndall effect of (b-d)  $\text{NiFe-LDH}$  and (e-g)  $\text{CeO}_{2-x}/\text{NiFe-LDH}$ .

2–3 nm were successfully decorated on ultrathin  $\text{NiFe-LDH}$  nanosheets, as well confirmed by HRTEM lattice image with lattice spacings of 0.31 nm for (111) facet of  $\text{CeO}_2$  nanoparticles and 0.26 nm for (012) facet of  $\text{NiFe-LDH}$  nanosheets (Fig. 2d). The  $\text{CeO}_2$  species in  $\text{CeO}_{2-x}/\text{NiFe-LDH}$  were further confirmed by X-ray diffraction (XRD) (Fig. S1). In-situ growing  $\text{CeO}_2$  on  $\text{NiFe-LDH}$  would benefit from the use of high-valence  $\text{Ce}^{4+}$  precursor. Indeed, the larger ionic radius and higher valency for  $\text{Ce}^{4+}$  (87 pm) than  $\text{Ni}^{2+}$  (69 pm) and  $\text{Fe}^{3+}$  (55 pm) prohibit the entrance of  $\text{Ce}^{4+}$  into the crystal lattice of  $\text{NiFe-LDH}$  [17]. The elemental mapping images of  $\text{CeO}_{2-x}/\text{NiFe-LDH}$  were also obtained to reveal the elemental distribution. The element mapping (Fig. 2e)

demonstrates the uniform distribution of Ce elements on single-layered  $\text{NiFe-LDH}$ .

X-ray photoelectron spectroscopy (XPS) was used to identify the interactions between  $\text{CeO}_{2-x}$  and  $\text{NiFe-LDH}$ . After growing  $\text{CeO}_{2-x}$  on  $\text{NiFe-LDH}$  (Fig. 3a and b), about 0.4 eV and 0.6 eV increase in  $\text{Ni } 2p_{3/2}$  (856.6 eV for  $\text{CeO}_{2-x}/\text{NiFe-LDH}$  and 856.2 eV for  $\text{NiFe-LDH}$ ) and  $\text{Fe } 2p_{3/2}$  (713.5 eV for  $\text{CeO}_{2-x}/\text{NiFe-LDH}$  and 712.9 eV for  $\text{NiFe-LDH}$ ) binding energies were observed, implying that the existence of  $\text{CeO}_2$  makes the Fe and Ni of  $\text{NiFe-LDH}$  tend to loss electrons. The binding energy of  $\text{Ce } 3d$  is about 0.5 eV lower for  $\text{CeO}_{2-x}/\text{NiFe-LDH}$  than  $\text{CeO}_2$ , suggesting that  $\text{CeO}_{2-x}$  nanoparticles can extract electrons from Ni and



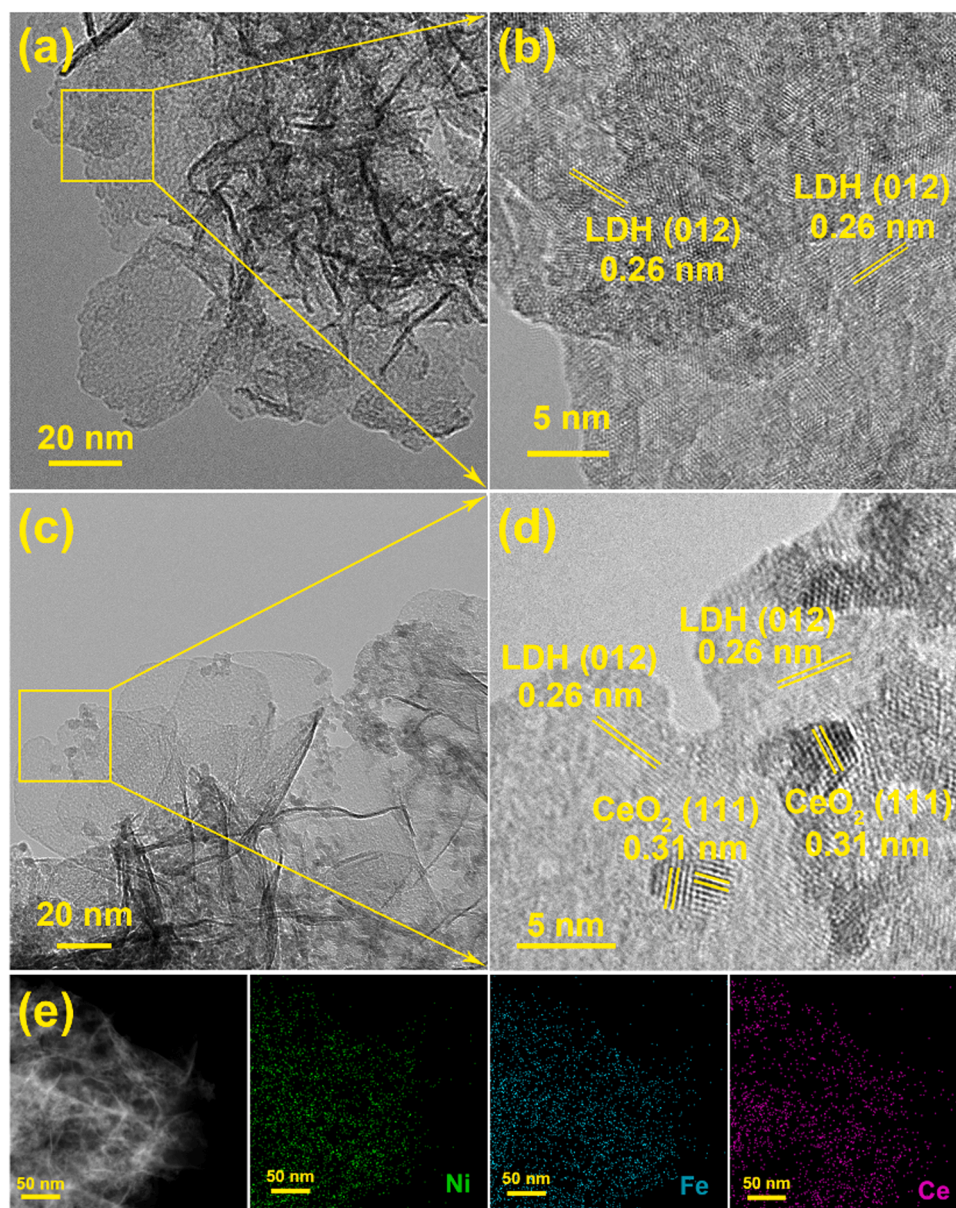


**Fig. 2.** TEM and HRTEM crystal lattice images of (a, b) NiFe-LDH and (c, d) CeO<sub>2-x</sub>/NiFe-LDH. (e) HAADF and element mapping of CeO<sub>2-x</sub>/NiFe-LDH.

Fe sites in NiFe-LDH layers (Fig. 3c). Indeed, the work function of CeO<sub>2</sub> (4.69 eV) [38–40] is much higher than that of NiFe-LDH (3.79 eV) [41–44], indicating that electrons preferentially transfer from NiFe-LDH to CeO<sub>2-x</sub>. Except the Ni/Fe-OH at 531.5 eV and adsorbed H<sub>2</sub>O at 533.6 eV for NiFe-LDH, the O 1s core-level spectrum of CeO<sub>2-x</sub>/NiFe-LDH (Fig. 3d) exhibited peaks at 529.3 eV for Ce-O, at 530.7 eV for Ni/Fe-O and at 532.6 eV for oxygen vacancies (O<sub>Vs</sub>), respectively [35, 45]. In addition, the content of Ni/Fe-OH is obviously lower for CeO<sub>2-x</sub>/NiFe-LDH than NiFe-LDH. These facts mean that, during the formation of CeO<sub>2-x</sub>/NiFe-LDH assembly, the Ce<sup>4+</sup> ions with completely unoccupied 4f orbitals are able to replace protons to strongly coordinate with the bridging oxygens with lone-pair electrons on NiFe-LDH layers [46], thus reducing the content of Ni/Fe-OH due to forming -Ni/Fe-O-Ce- species at the interface between CeO<sub>2-x</sub> and NiFe-LDH. The formation of Ni/Fe-O species further supports that the strong interactions between CeO<sub>2-x</sub> and NiFe-LDH is from the electron exchange effect of Ni/Fe-O-Ce configuration.

### 3.2. Electrochemical OER activities

The linear sweep voltammetry (LSV) was performed in 1.0 M KOH electrolyte to check the OER activity for as-prepared samples. We first optimized the content of CeO<sub>2-x</sub> on NiFe-LDH and the corresponding samples were denoted as y-CeO<sub>2-x</sub>/NiFe-LDH (y indicates the micro-mole content of Ce(NH<sub>4</sub>)<sub>2</sub>(NO<sub>3</sub>)<sub>6</sub>, y = 50, 150, and 300). As for y-CeO<sub>2-x</sub>/NiFe-LDH, the optimized usage of Ce(NH<sub>4</sub>)<sub>2</sub>(NO<sub>3</sub>)<sub>6</sub> was 150 μmol (Fig. 4a). At a current density of 10 mA cm<sup>-2</sup>, 150-CeO<sub>2-x</sub>/NiFe-LDH shows the lowest overpotential of 216 mV according to the negative-going scanning curve of cyclic voltammetry (CV) measurements (Fig. S2), which is 40 mV lower than pure single-layered NiFe-LDH (256 mV). Additionally, at the potential of 1.6 V vs. RHE, the current density of 150-CeO<sub>2-x</sub>/NiFe-LDH reaches to 250 mA cm<sup>-2</sup>, which is three times higher than that of NiFe-LDH (Fig. 4a). The Tafel slope of 150-CeO<sub>2-x</sub>/NiFe-LDH is 74.1 mV dec<sup>-1</sup>, which is much lower than 50-CeO<sub>2-x</sub>/NiFe-LDH (83.6 mV dec<sup>-1</sup>), 300-CeO<sub>2-x</sub>/NiFe-LDH (107.1 mV dec<sup>-1</sup>), and NiFe-LDH (117.9 mV dec<sup>-1</sup>) (Fig. 4b), indicating the favorable OER kinetics and excellent catalytic activity of 150-

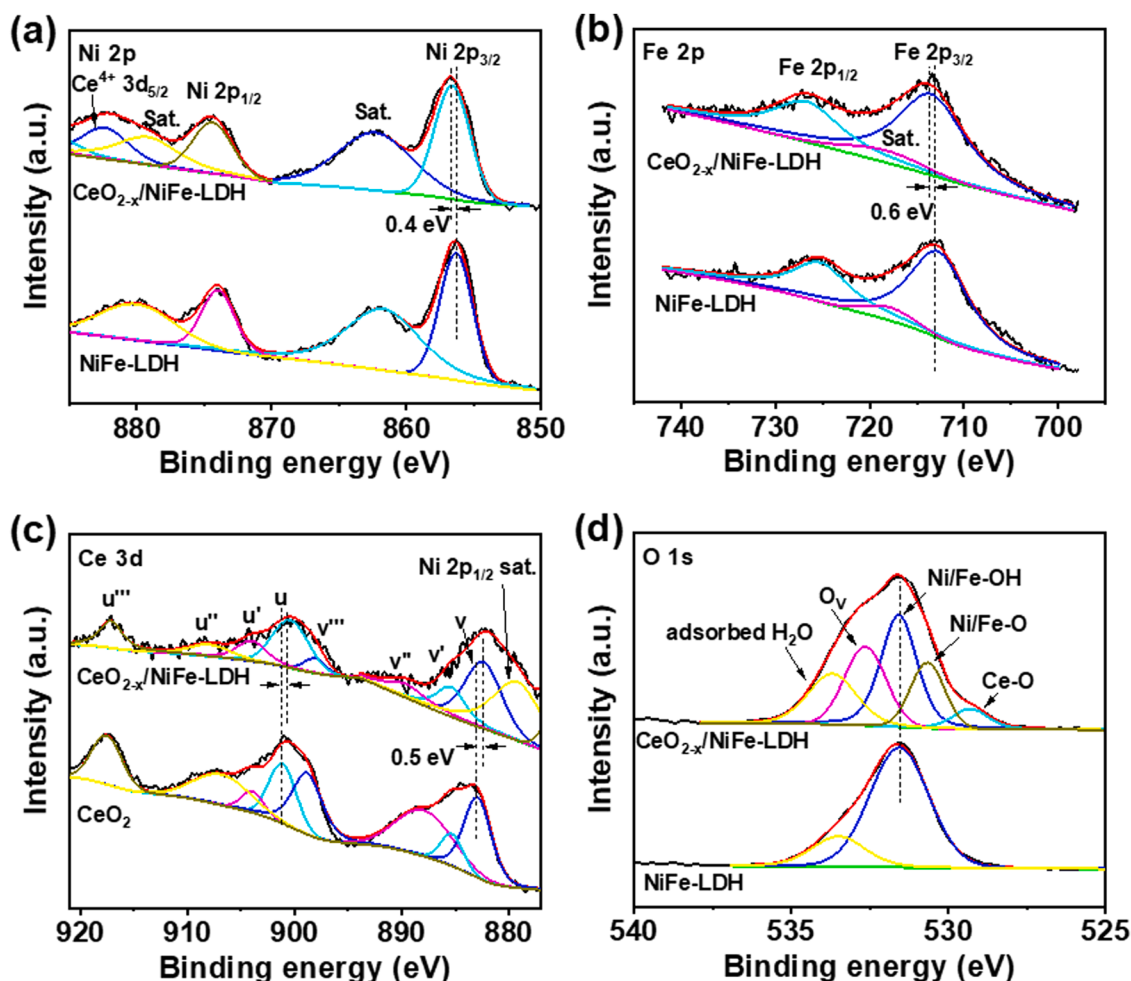


**Fig. 3.** The core-level XPS spectra before OER testing. (a) The Ni 2p XPS spectra for  $\text{CeO}_{2-x}/\text{NiFe-LDH}$  and  $\text{NiFe-LDH}$ . (b) The Fe 2p XPS spectra for  $\text{CeO}_{2-x}/\text{NiFe-LDH}$  and  $\text{NiFe-LDH}$ . (c) The Ce 3d XPS spectra for  $\text{CeO}_{2-x}/\text{NiFe-LDH}$  and  $\text{CeO}_2$ . (d) The O 1s XPS spectra for  $\text{CeO}_{2-x}/\text{NiFe-LDH}$  and  $\text{NiFe-LDH}$ .

$\text{CeO}_{2-x}/\text{NiFe-LDH}$ . As listed in Table S1, the OER performances of 150- $\text{CeO}_{2-x}/\text{NiFe-LDH}$  exceeded most of the previously reported  $\text{NiFe-LDH}$ -based catalysts. The stability of 150- $\text{CeO}_{2-x}/\text{NiFe-LDH}$  has also been evaluated, the chronopotentiometry was used to get v-t curve in Fig. 4c. After the 10 h test, it can still maintain a constant voltage of 1.48 V. Moreover, the TEM images of 150- $\text{CeO}_{2-x}/\text{NiFe-LDH}$  after OER stability test in Fig. S3 demonstrated the maintenance of the nanosheet morphology and lattice fringe of the  $\text{NiFe-LDH}$  and  $\text{CeO}_{2-x}$ , which also proved the good stability of 150- $\text{CeO}_{2-x}/\text{NiFe-LDH}$ .

As shown in Fig. 4d, the ECSA-normalized LSV curves of y- $\text{CeO}_{2-x}/\text{NiFe-LDH}$  were similar, but they were higher than that of  $\text{NiFe-LDH}$ , indicating that  $\text{CeO}_{2-x}$  decoration strongly enhanced the intrinsic OER activity of  $\text{NiFe-LDH}$ . The ECSA of 150- $\text{CeO}_{2-x}/\text{NiFe-LDH}$  ( $1.80 \text{ cm}^2$ ) is higher than those of 50- $\text{CeO}_{2-x}/\text{NiFe-LDH}$  ( $1.40 \text{ cm}^2$ ), 300- $\text{CeO}_{2-x}/\text{NiFe-LDH}$  ( $1.10 \text{ cm}^2$ ), and  $\text{NiFe-LDH}$  ( $1.45 \text{ cm}^2$ ), indicating the more active-site exposure of 150- $\text{CeO}_{2-x}/\text{NiFe-LDH}$ . Indeed, TEM observations (Fig. S5) suggested that the excessive  $\text{CeO}_{2-x}$  covers the active sites on  $\text{NiFe-LDH}$ . Electrochemical impedance spectroscopy (EIS) was used to monitor the charge transfer during OER. The Nyquist plots of  $\text{NiFe-LDH}$  without and with  $\text{CeO}_{2-x}$  were recorded at an OER potential of 1.51 V and were fitted by typical Randle's equivalent circuit, as shown in Fig. 4e. Two semicircles were observed in Nyquist plots. The fitting equivalent circuit was composed of electrolyte-catalyst electrical connection resistance ( $R_s$ ), and electron transfer resistance and capacitance in bulk of catalyst ( $R_{\text{bulk}}$ ,  $C_{\text{bulk}}$ ) and at OER interface ( $R_{\text{ct}}$ ,  $C_{\text{ct}}$ ). The semicircle at the high-frequency region can be attributed to bulk transfer resistance ( $R_{\text{bulk}}$ ), mainly related to the  $\text{Ni}^{2+}/\text{Ni}^{3+}$  oxidation, as well

demonstrated by the  $\text{Ni}^{2+}/\text{Ni}^{3+}$  oxidation wave at 1.35–1.48 V in LSV curves (Fig. 4a) [47]. The semicircle at the low-frequency region originated from charge transfer resistance ( $R_{\text{ct}}$ ), related to the OER kinetics at catalyst-electrolyte interface. As listed in Table S2, the 150- $\text{CeO}_{2-x}/\text{NiFe-LDH}$  electrode exhibited the lowest  $R_{\text{bulk}}$  and  $R_{\text{ct}}$ , suggesting that dispersing moderate amounts of  $\text{CeO}_{2-x}$  on  $\text{NiFe-LDH}$  induced efficient electron transfer during OER. An excessive or insufficient dose of  $\text{CeO}_{2-x}$  will induce the screening of active species or insignificant promotion effect for electron transfer, respectively, as indicated by the higher  $R_{\text{bulk}}$  and  $R_{\text{ct}}$ . The pure  $\text{CeO}_2$  exhibited the significantly larger  $R_{\text{bulk}}$  and  $R_{\text{ct}}$  than the y- $\text{CeO}_{2-x}/\text{NiFe-LDH}$  electrodes, well revealing that the  $\text{CeO}_2$  is not the OER active species.

The promotion effect of charge transfer by  $\text{CeO}_{2-x}$  is further visualized by Bode plots (Fig. 4f). Bode plots described two electrochemical processes on y- $\text{CeO}_{2-x}/\text{NiFe-LDH}$  electrodes, respectively exhibiting phase peak at high frequency region ( $10^2$ – $10^4 \text{ Hz}$ ) for electron transfer in - $\text{Ni/Fe-O-Ce-}$  configuration and the phase peak at low frequency region ( $10^0$ – $10^1 \text{ Hz}$ ) for electron transfer from OER intermediates to the active species [48,49]. Compared to  $\text{NiFe-LDH}$ , the peak frequency of y- $\text{CeO}_{2-x}/\text{NiFe-LDH}$  slightly shifted toward higher frequency region. This suggested that the  $\text{CeO}_{2-x}$  modification promotes the electron transfer in/at bulk/interface of 50- $\text{CeO}_{2-x}/\text{NiFe-LDH}$  or 150- $\text{CeO}_{2-x}/\text{NiFe-LDH}$ . However, the peak frequency of 300- $\text{CeO}_{2-x}/\text{NiFe-LDH}$  is different from those of 50- $\text{CeO}_{2-x}/\text{NiFe-LDH}$  or 150- $\text{CeO}_{2-x}/\text{NiFe-LDH}$ , resulting from that the excessive  $\text{CeO}_{2-x}$  covers the active sites on  $\text{NiFe-LDH}$ .

After OER, the XPS analysis revealed that the Fe and Ni ions in

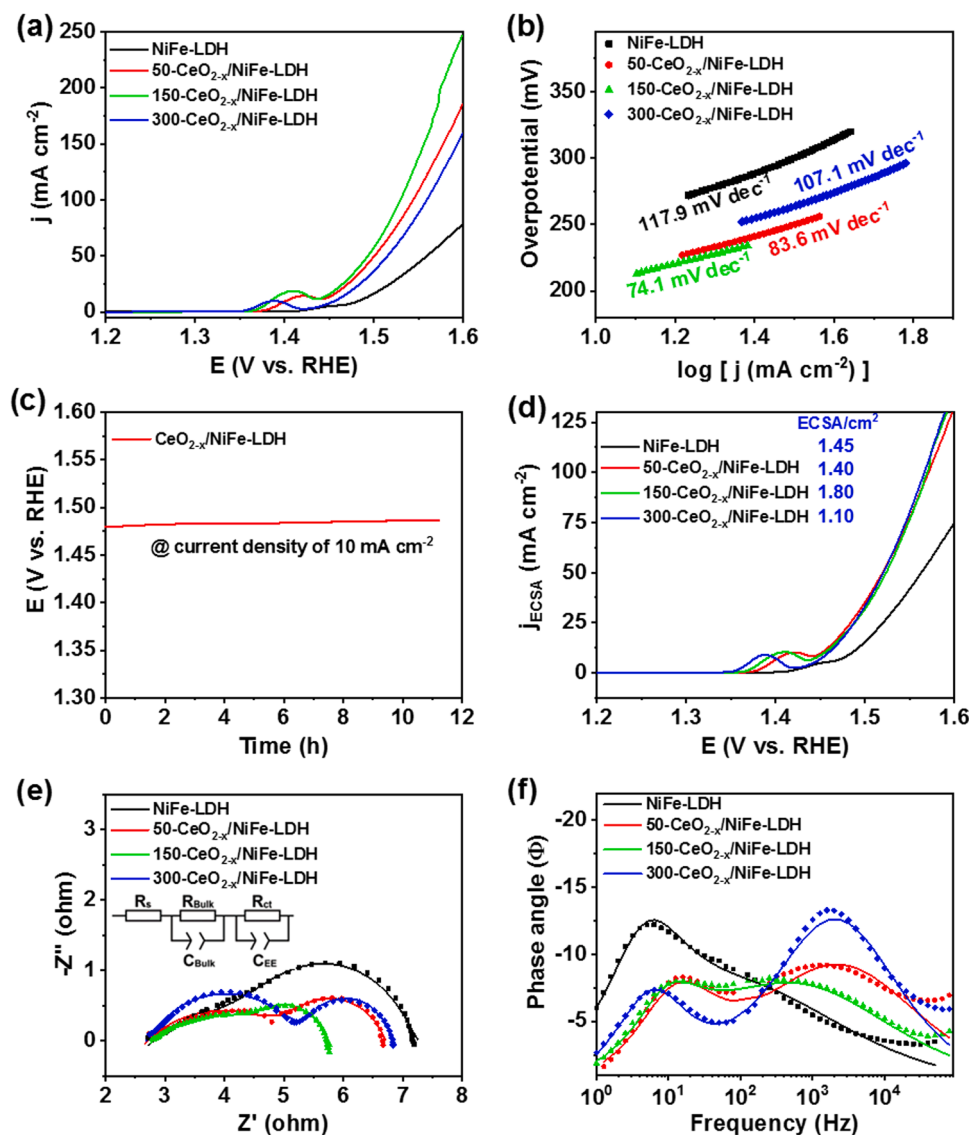


**Fig. 4.** (a) LSV curves and (b) Tafel plots of  $\gamma$ -CeO<sub>2-x</sub>/NiFe-LDHs with different Ce amounts. (c) The chronopotentiometry plot of 150-CeO<sub>2-x</sub>/NiFe-LDH at 10 mA cm<sup>-2</sup>. (d) LSV curves normalized by ECSA of the as-prepared samples. The ECSA was calculated by double-layer capacitance, as shown in Fig. S4. (e) Nyquist plots and (f) Bode plots at an overpotential of 280 mV. Insets show the equivalent circuit.

CeO<sub>2-x</sub>/NiFe-LDH tend to gain electrons to stay at a relatively lower valency (Fig. S6). In contrast, the Ce ions in CeO<sub>2-x</sub>/NiFe-LDH like to lose electrons. For the OER occurrence on NiFe-LDH, although the charge transfer and active sites are still under discussion, the theoretical and experimental results tend to believe that the charge transfer is a result of synergy of Ni and Fe and the Fe sites directly interact with the OER intermediates [10–12,50,51]. In our case, the OER would occur at the exposed junction interface between CeO<sub>2-x</sub> particles and NiFe-LDH nanosheets. The valency decrease in Fe and Ni ions may suggest that the CeO<sub>2-x</sub>/NiFe-LDH follows the similar OER catalysis mechanism to the NiFe-LDH. The Fe sites are able to strongly capture the OER intermediates and transfer electrons to Ni sites via the exchange effects of Fe-O-Ni configurations. The increased valency for Ce ion during OER probably implied that the Ce ions as strong electron acceptor take part in the electrons from OER intermediates to external circuit via the exchange effects of -Ni/Fe-O-Ce- configurations, as shown in Fig. 5a. The existence of O<sub>V</sub>s in the CeO<sub>2-x</sub> suggests a high ion conductive ability via the Ce<sup>3+</sup>/Ce<sup>4+</sup> redox couple to transfer electrons. Indeed, the content of Ce<sup>3+</sup> species in CeO<sub>2-x</sub>/NiFe-LDH was calculated according to the area of four-pair spin-orbital doublet peaks (Fig. 3c): v/u, v''/u'', and

v'''/u''' peaks for Ce<sup>4+</sup> 3d orbitals and v'/u' peaks for Ce<sup>3+</sup> 3d orbitals [34–36]. After OER, the content of Ce<sup>3+</sup> species decreased from approximately 20.84–5.82% (Fig. S6c).

More importantly, after OER, the HRTEM crystal lattice image (Fig. S3) confirmed that the catalyst keeps the crystal structure of Ni<sub>1-x</sub>Fe<sub>x</sub>(OH)<sub>2</sub>. This fact indicated that there is no Ni<sub>1-x</sub>Fe<sub>x</sub>(OH)<sub>2</sub>/Ni<sub>1-x</sub>Fe<sub>x</sub>OOH interconversion during OER on CeO<sub>2-x</sub>/NiFe-LDH. As for pure NiFe-LDH, Ni<sup>2+</sup> in Ni<sub>1-x</sub>Fe<sub>x</sub>(OH)<sub>2</sub> would be oxidized to Ni<sup>3+</sup> in Ni<sub>1-x</sub>Fe<sub>x</sub>OOH by coupling with a deprotonation process [52]. However, in CeO<sub>2-x</sub>/NiFe-LDH, thanks to the unique redox properties of Ce<sup>3+</sup>/Ce<sup>4+</sup> in CeO<sub>2-x</sub>, electrons at Ni<sup>2+</sup> are transferred to Ce<sup>4+</sup> sites via Ni-O-Ce exchange effects [25,53,54] due to the higher work function for CeO<sub>2</sub> than that for NiFe-LDH. This interaction decreased the energy barrier of Ni<sup>2+</sup>/Ni<sup>3+</sup> oxidation without the deprotonation process. Indeed, the onset potential of Ni<sup>2+</sup>/Ni<sup>3+</sup> oxidation wave gradually decreased with the content increase of CeO<sub>2-x</sub> (Fig. 4a), indicating that CeO<sub>2-x</sub> can directly accept the electrons from Ni<sup>2+</sup> to promote the Ni<sup>2+</sup>/Ni<sup>3+</sup> oxidation. This accelerated electron transfer would contribute to the higher OER activity [13,55,56].

Accordingly, we can conclude the OER mechanism on CeO<sub>2-x</sub>/NiFe-



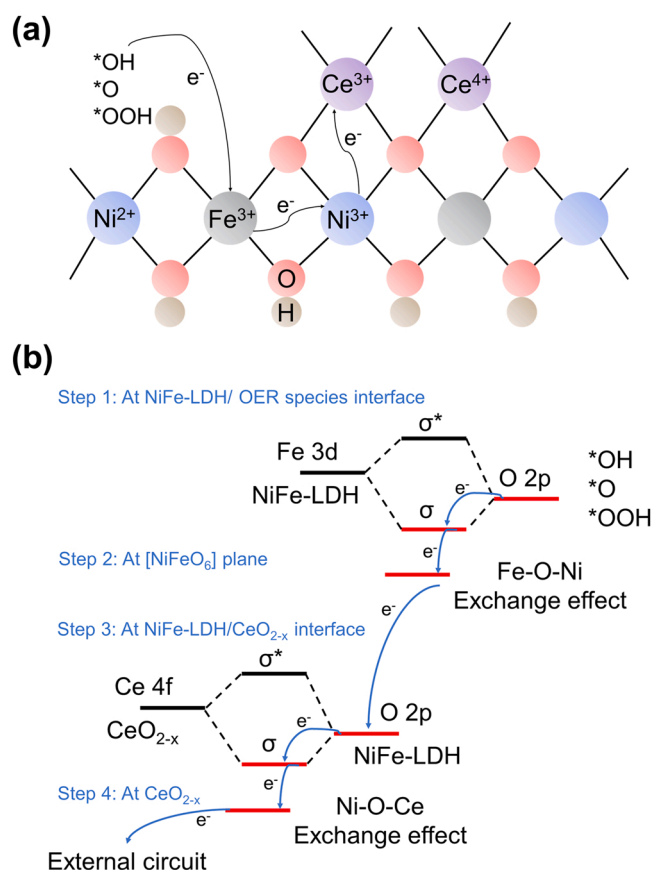


**Fig. 5.** (a) Proposed mechanism of enhanced OER performance at the interface of CeO<sub>2-x</sub>/NiFe-LDH. (b) electron transferring path during OER process.

LDH. As shown in Fig. 5b, after adsorbing the OER intermediates, the binding states ( $\sigma$  states) comprising of O 2p-(Fe, Ni) 3d hybridized orbitals between OER intermediates (\*OH, \*O, \*OOH) and active species are the energy transfer channels. At the OER potentials, the electrons are extracted by external electric field from OER intermediates to inject into Fe 3d orbitals of NiFe-LDH via the  $\sigma$  states [57,58]. Subsequently, the electrons are transferred to Ni sites via the Fe-O-Ni exchange effects, reach to CeO<sub>2-x</sub> particles via the exchange effect of Ni/Fe-O-Ce configuration, and finally are extracted to external circuit.

#### 4. Conclusions

In summary, as an efficient OER electrocatalyst, CeO<sub>2-x</sub> decorated single-layered NiFe-LDH was prepared by a one-step co-precipitation method. CeO<sub>2-x</sub> nanoparticles, with strong interaction effect on the interface with NiFe-LDH, acted as electron acceptors to extract electrons from Ni sites by the exchange effect of Ni-O-Ce, promoting the oxidation of Ni<sup>2+</sup> to Ni<sup>3+</sup> by avoiding deprotonation reaction of Ni<sub>1-x</sub>Fe<sub>x</sub>(OH)<sub>2</sub>/Ni<sub>1-x</sub>Fe<sub>x</sub>OOH phase change. The single-layered nanosheet structure benefits for electron transfer from the heterojunction of Ni-O-Ce to the external circuit. As a result, the CeO<sub>2-x</sub>/NiFe-LDH tested on the plate carbon paper electrode exhibited excellent OER performance with a low overpotential of 216 mV at the current density of 10 mA cm<sup>-2</sup> and a Tafel slope of 74.1 mV dec<sup>-1</sup>. This work provided a novel orientation to modify the NiFe-based materials for better OER catalytic performance and provided a new insight into the interaction between CeO<sub>2-x</sub> and NiFe-LDH.

#### CRedit authorship contribution statement

The work was conceived and designed by Shicheng Yan, Yu Du and

Depei Liu. Yu Du accomplished the experiments, wrote the manuscript. Depei Liu assisted to accomplish the experiments and revised the manuscript. Taozhu Li finished the atomic force microscopy characterization and analysis. Yuandong Yan and Yan Liang provided constructive suggestions for characterization and electrochemical testing results. Shicheng Yan and Zhigang Zou in charge of Data curation, Funding acquisition, Project administration, Validation; and all authors discussed the results.

#### Declaration of Competing Interest

The authors declare that they have no known competing financial interests or personal relationships that could have appeared to influence the work reported in this paper.

#### Acknowledgements

This work was supported primarily by the National Natural Science Foundation of China, China (Grant Nos. 51872135, 21633004, 21603098, 51572121, and 51902137), the Fundamental Research Funds for the Central Universities, China (Grant Nos. 021314380084 and 021314380133), the Natural Science Foundation of Jiangsu Province, China (Grant Nos BK20151383, BK20150580 and BK20151265).

#### Appendix A. Supporting information

Supplementary data associated with this article can be found in the online version at doi:10.1016/j.apcatb.2022.121146.

#### References

- [1] L.G. Li, P.T. Wang, Q. Shao, X.Q. Huang, Metallic nanostructures with low dimensionality for electrochemical water splitting, *Chem. Soc. Rev.* 49 (2020) 3072–3106.
- [2] J.S. Li, T. Hu, C.H. Wang, C.X. Guo, Surface-mediated iron on porous cobalt oxide with high energy state for efficient water oxidation electrocatalysis, *Green Energy Environ.* (2020), <https://doi.org/10.1016/j.gjee.2020.11.009>.
- [3] A. Zhang, Y. Liang, H. Zhang, Z. Geng, J. Zeng, Doping regulation in transition metal compounds for electrocatalysis, *Chem. Soc. Rev.* 50 (2021) 9817–9844.
- [4] D. Salvatore, C.P. Berlinguette, Voltage matters when reducing CO<sub>2</sub> in an electrochemical flow cell, *ACS Energy Lett.* 5 (2019) 215–220.
- [5] Q. Wang, L. Shang, R. Shi, X. Zhang, Y. Zhao, G.I.N. Waterhouse, L.Z. Wu, C. H. Tung, T. Zhang, NiFe layered double hydroxide nanoparticles on Co,N-codoped carbon nanoframes as efficient bifunctional catalysts for rechargeable zinc-air batteries, *Adv. Energy Mater.* 7 (2017), 1700467.
- [6] J. Li, C. Guo, C.M. Li, Recent advances of two-dimensional (2D) MXenes and phosphorene for high-performance rechargeable batteries, *ChemSusChem* 13 (2020) 1047–1070.
- [7] N.C.S. Selvam, L. Du, B.Y. Xia, P.J. Yoo, B. You, Reconstructed water oxidation electrocatalysts: the impact of surface dynamics on intrinsic activities, *Adv. Funct. Mater.* 31 (2021), 2008190.
- [8] X. Yang, Z. Zhao, Q. Shen, C. Xu, C. Shi, W. Cao, Y. Sun, B. Xu, Morphology and electronic modulation of composite nanosheets for electrocatalytic oxygen evolution through partial and in situ transformation of NiFe-LDH, *CrystEngComm* 23 (2021) 1572–1577.
- [9] Y. Du, D.P. Liu, S.C. Yan, T. Yu, Z.G. Zou, NiFe layered double hydroxides for oxygen evolution reaction, *Prog. Chem.* 32 (2020) 1386–1401.
- [10] J.F. Zhang, H.J. Zhang, Y. Huang, Electron-rich NiFe layered double hydroxides via interface engineering for boosting electrocatalytic oxygen evolution, *Appl. Catal. B Environ.* 297 (2021), 120453.
- [11] B.Q. Wang, X. Han, C. Guo, J. Jing, C. Yang, Y.P. Li, A.J. Han, D.S. Wang, J.F. Liu, Structure inheritance strategy from MOF to edge-enriched NiFe-LDH array for enhanced oxygen evolution reaction, *Appl. Catal. B Environ.* 298 (2021), 120580.
- [12] B. Zhang, L. Wang, Z. Cao, S.M. Kozlov, F.P.G. de Arquer, C.T. Dinh, J. Li, Z. Y. Wang, X.L. Zheng, L.S. Zhang, High-valence metals improve oxygen evolution reaction performance by modulating 3 d metal oxidation cycle energetics, *Nat. Catal.* 3 (2020) 985–992.
- [13] N. Li, D.K. Bediako, R.G. Hadt, D. Hayes, T.J. Kempa, F. von Cube, D.C. Bell, L. X. Chen, D.G. Nocera, Influence of iron doping on tetravalent nickel content in catalytic oxygen evolving films, *Proc. Natl. Acad. Sci. USA* 114 (2017) 1486–1491.
- [14] D.J. Zhou, X.Y. Xiong, Z. Cai, N.N. Han, Y. Jia, Q.X. Xie, X.X. Duan, T.H. Xie, X. L. Zheng, X.M. Sun, Flame-engraved nickel-iron layered double hydroxide nanosheets for boosting oxygen evolution reactivity, *Small Methods* 2 (2018), 1800083.
- [15] J. Xie, X. Zhang, H. Zhang, J. Zhang, S. Li, R. Wang, B. Pan, Y. Xie, Intralayered ostwald ripening to ultrathin nanomesh catalyst with robust oxygen-evolving performance, *Adv. Mater.* 29 (2017), 1604765.

- [16] Y.Y. Wang, M. Qiao, Y.F. Li, S.Y. Wang, Tuning surface electronic configuration of NiFe LDHs nanosheets by introducing cation vacancies (Fe or Ni) as highly efficient electrocatalysts for oxygen evolution reaction, *Small* 14 (2018), 1800136.
- [17] H. Xu, B. Wang, C. Shan, P. Xi, W. Liu, Y. Tang, Ce-doped NiFe-layered double hydroxide ultrathin nanosheets/nanocarbon hierarchical nanocomposite as an efficient oxygen evolution catalyst, *ACS Appl. Mater. Interfaces* 10 (2018) 6336–6345.
- [18] D.J. Zhou, Z. Cai, X.D. Lei, W.L. Tian, Y.M. Bi, Y. Jia, N.N. Han, T.F. Gao, Q. Zhang, Y. Kuang, J.Q. Pan, X.M. Sun, X. Duan, NiCoFe-layered double hydroxides/N-doped graphene oxide array colloid composite as an efficient bifunctional catalyst for oxygen electrocatalytic reactions, *Adv. Energy Mater.* 8 (2018), 1701905.
- [19] J.W. Huang, G.W. Hu, Y. Ding, M.C. Pang, B. Ma, Mn-doping and NiFe layered double hydroxide coating: effective approaches to enhancing the performance of  $\alpha$ -Fe<sub>2</sub>O<sub>3</sub> in photoelectrochemical water oxidation, *J. Catal.* 340 (2016) 261–269.
- [20] K.N. Dinh, P.L. Zheng, Z.F. Dai, Y. Zhang, R. Dangol, Y. Zheng, B. Li, Y. Zong, Q. Y. Yan, Ultrathin porous NiFeV ternary layer hydroxide nanosheets as a highly efficient bifunctional electrocatalyst for overall water splitting, *Small* 14 (2018), 1703257.
- [21] X. Zhang, Y.F. Zhao, Y.X. Zhao, R. Shi, G.L.N. Waterhouse, T.R. Zhang, A simple synthetic strategy toward defect-rich porous monolayer NiFe-layered double hydroxide nanosheets for efficient electrocatalytic water oxidation, *Adv. Energy Mater.* 9 (2019), 1900881.
- [22] Y.F. Zhao, X. Zhang, X.D. Jia, G.L.N. Waterhouse, R. Shi, X.R. Zhang, F. Zhan, Y. Tao, L.Z. Wu, C.H. Tung, D. O'Hare, T.R. Zhang, Sub-3 nm ultrafine monolayer layered double hydroxide nanosheets for electrochemical water oxidation, *Adv. Energy Mater.* 8 (2018), 1703585.
- [23] F. Song, X. Hu, Exfoliation of layered double hydroxides for enhanced oxygen evolution catalysis, *Nat. Commun.* 5 (2014) 4477.
- [24] T. Li, X.J. Hao, S. Bai, Y.F. Zhao, Y.F. Song, Controllable synthesis and scale-up production prospect of monolayer layered double hydroxide nanosheets, *Acta Phys. Chim. Sin.* 36 (2020), 1912005.
- [25] Q.B. Dong, C. Shuai, Z.L. Mo, N.J. Liu, G.G. Liu, J. Wang, H.B. Pei, Q.Q. Jia, W. T. Liu, X.D. Guo, CeO<sub>2</sub> nanoparticles@ NiFe-LDH nanosheet heterostructure as electrocatalysts for oxygen evolution reaction, *J. Solid State Chem.* 296 (2021), 121967.
- [26] J.H. Cai, J.G. Huang, S.C. Xu, L. Yuan, X.R. Huang, Z.P. Huang, C. Zhang, Nickel iron carbonate hydroxide hydrate decorated with CeO<sub>2</sub> for highly efficient oxygen evolution reaction, *J. Solid State Electrochem.* 23 (2019) 3449–3458.
- [27] X. Long, H. Lin, D. Zhou, Y.M. An, S.H. Yang, Enhancing full water-splitting performance of transition metal bifunctional electrocatalysts in alkaline solutions by tailoring CeO<sub>2</sub>-transition metal oxides-Ni nanointerfaces, *ACS Energy Lett.* 3 (2018) 290–296.
- [28] D. Liu, Y. Du, T. Li, H. Zhang, D. Liu, W. Zhang, H. Tang, Y. Hou, J. Li, S. Yan, T. Yu, Z. Zou, One-step synthesis of IrO<sub>2</sub>-decorated ultrathin NiFe LDH nanosheets for efficient oxygen evolution reaction, *Chem. Commun.* 56 (2020) 11465–11468.
- [29] Y. Zhang, S. Zhao, J. Feng, S.Y. Song, W.D. Shi, D. Wang, H.J. Zhang, Unraveling the physical chemistry and materials science of CeO<sub>2</sub>-based nanostructures, *Chem* 7 (2021) 2022–2059.
- [30] W. Yang, X. Wang, S. Song, H. Zhang, Syntheses and applications of noble-metal-free CeO<sub>2</sub>-based mixed-oxide nanocatalysts, *Chem* 5 (2019) 1743–1774.
- [31] J.D. Wang, X. Xiao, Y. Liu, K.M. Pan, H. Pang, S.Z. Wei, The application of CeO<sub>2</sub>-based materials in electrocatalysis, *J. Mater. Chem. A* 7 (2019) 17675–17702.
- [32] G.L. Lu, H.Y. Zheng, J.J. Lv, G. Wang, X.B. Huang, Review of recent research work on CeO<sub>2</sub>-based electrocatalysts in liquid-phase electrolytes, *J. Power Sources* 480 (2020), 229091.
- [33] C.G. Silva, Y. Bouizi, V. Fornés, H. García, Layered double hydroxides as highly efficient photocatalysts for visible light oxygen generation from water, *J. Am. Chem. Soc.* 131 (2009) 13833–13839.
- [34] A.D. Liyanage, S.D. Perera, K. Tan, Y. Chabal, K.J. Balkus, Synthesis, characterization, and photocatalytic activity of Y-doped CeO<sub>2</sub> nanorods, *ACS Catal.* 4 (2014) 577–584.
- [35] K. Herget, P. Hubach, S. Pusch, P. Deglmann, H. Gotz, T.E. Gorelik, I.A. Gural'skiy, F. Pfizner, T. Link, S. Schenk, M. Panthofer, V. Ksenofontov, U. Kolb, T. Opatz, R. Andre, W. Tremel, Haloperoxidase mimicry by CeO<sub>2-x</sub> nanorods combats biofouling, *Adv. Mater.* 29 (2017), 1603823.
- [36] Y. Xue, Q.F. Luan, D. Yang, X. Yao, K.B. Zhou, Direct evidence for hydroxyl radical scavenging activity of cerium oxide nanoparticles, *J. Phys. Chem. C* 115 (2011) 4433–4438.
- [37] T. Hibino, Delamination of layered double hydroxides containing amino acids, *Chem. Mater.* 16 (2004) 5482–5488.
- [38] H.F. Wardenga, A. Klein, Surface potentials of (111), (110) and (100) oriented CeO<sub>2-x</sub> thin films, *Appl. Surf. Sci.* 377 (2016) 1–8.
- [39] Y.J. Chen, G. Xiao, T.S. Wang, F. Zhang, Y. Ma, P. Gao, C.L. Zhu, E. Zhang, Z. Xu, Q. H. Li, Synthesis and enhanced gas sensing properties of crystalline CeO<sub>2</sub>/TiO<sub>2</sub> core/shell nanorods, *Appl. Catal. B Environ.* 156 (2011) 867–874.
- [40] T. Yu, B. Lim, Y. Xia, Aqueous-phase synthesis of single-crystal ceria nanosheets, *Angew. Chem. Int. Ed.* 122 (2010) 4586–4589.
- [41] J. Yan, X. Zhang, W. Zheng, L.Y.S. Lee, Interface engineering of a 2D-C<sub>3</sub>N<sub>4</sub>/NiFe-LDH heterostructure for highly efficient photocatalytic hydrogen evolution, *ACS Appl. Mater. Interfaces* 13 (2021) 24723–24733.
- [42] Y.H. Ma, D.X. Xu, W.R. Chen, Y.M. Tang, X. Wang, L.S. Li, J. Wang, Oxygen-vacancy-embedded 2D/2D NiFe-LDH/MXene Schottky heterojunction for boosted photodegradation of norfloxacin, *Appl. Surf. Sci.* 572 (2022), 151432.
- [43] J. Xu, Z. Li, D. Chen, S. Yang, K. Zheng, J. Ruan, Y. Wu, H. Zhang, J. Chen, F. Xie, Y. Jin, N. Wang, H. Meng, Porous indium tin oxide-supported NiFe LDH as a highly active electrocatalyst in the oxygen evolution reaction and flexible zinc-air batteries, *ACS Appl. Mater. Interfaces* 13 (2021) 48774–48783.
- [44] F.Y. Ning, M.F. Shao, S.M. Xu, Y. Fu, R.K. Zhang, M. Wei, D.G. Evans, X. Duan, TiO<sub>2</sub>/graphene/NiFe-layered double hydroxide nanorod array photoanodes for efficient photoelectrochemical water splitting, *Energy Environ. Sci.* 9 (2016) 2633–2643.
- [45] G. Liu, M.H. Wang, Y. Wu, N. Li, F. Zhao, Q. Zhao, J.P. Li, 3D porous network heterostructure NiCe@NiFe electrocatalyst for efficient oxygen evolution reaction at large current densities, *Appl. Catal. B Environ.* 260 (2020), 118199.
- [46] L. Yao, J. Gu, W. Wang, T. Li, D. Ma, Q. Liu, W. Zhang, W. Abbas, A. Bahadoran, D. Zhang, Ce<sup>4+</sup> as a facile and versatile surface modification reagent for templated synthesis in electrical applications, *Nanoscale* 11 (2019) 2138–2142.
- [47] T. Nakagawa, N.S. Bjorge, R.W. Murray, Electrogenated IrO<sub>x</sub> nanoparticles as dissolved redox catalysts for water oxidation, *J. Am. Chem. Soc.* 131 (2009) 15578–15579.
- [48] F. Lyu, Y. Bai, Q. Wang, L. Wang, X. Zhang, Y. Yin, Phase-controllable synthesis of cobalt hydroxide for electrocatalytic oxygen evolution, *Dalton Trans.* 46 (2017) 10545–10548.
- [49] S.F. Hung, Y.Y. Hsu, C.J. Chang, C.S. Hsu, N.T. Suen, T.S. Chan, H.M. Chen, Unraveling geometrical site confinement in highly efficient iron-doped electrocatalysts toward oxygen evolution reaction, *Adv. Energy Mater.* 8 (2018), 1701686.
- [50] J.Y. Chen, L. Dang, H. Liang, W. Bi, J.B. Gerken, S. Jin, E.E. Alp, S.S. Stahl, Operando analysis of NiFe and Fe oxyhydroxide electrocatalysts for water oxidation: detection of Fe<sup>4+</sup> by Mossbauer spectroscopy, *J. Am. Chem. Soc.* 137 (2015) 15090–15093.
- [51] H. Xiao, H. Shin, W.A. Goddard, Synergy between Fe and Ni in the optimal performance of (Ni, Fe)OOH catalysts for the oxygen evolution reaction, *Proc. Natl. Acad. Sci. USA* 115 (2018) 5872–5877.
- [52] X.Z. Su, Y. Wang, J. Zhou, S.Q. Gu, J. Li, S. Zhang, Operando spectroscopic identification of active sites in NiFe prussian blue analogues as electrocatalysts: activation of oxygen atoms for oxygen evolution reaction, *J. Am. Chem. Soc.* 140 (2018) 11286–11292.
- [53] H.S. Jadhav, A. Roy, B.Z. Desalegan, J.G. Seo, An advanced and highly efficient Ce assisted NiFe-LDH electrocatalyst for overall water splitting, *Sustain. Energy Fuels* 4 (2020) 312–323.
- [54] M. Liu, K.A. Min, B. Han, L.Y.S. Lee, Interfacing or doping? Role of Ce in highly promoted water oxidation of NiFe-layered double hydroxide, *Adv. Energy Mater.* 11 (2021), 2101281.
- [55] M.W. Louie, A.T. Bell, An investigation of thin-film Ni-Fe oxide catalysts for the electrochemical evolution of oxygen, *J. Am. Chem. Soc.* 135 (2013) 12329–12337.
- [56] S. Klaus, Y. Cai, M.W. Louie, L. Trotochaud, A.T. Bell, Effects of Fe electrolyte impurities on Ni (OH)<sub>2</sub>/NiOOH structure and oxygen evolution activity, *J. Phys. Chem. C* 119 (2015) 7243–7254.
- [57] Y. Liang, J. Wang, D.P. Liu, L. Wu, T.Z. Li, S.C. Yan, Q. Fan, K. Zhu, Z.G. Zou, Ultrafast Fenton-like reaction route to FeOOH/NiFe-LDH heterojunction electrode for efficient oxygen evolution reaction, *J. Mater. Chem. A* 9 (2021) 21785–21791.
- [58] Y.M. Sun, S.N. Sun, H.T. Yang, S.B. Xi, J. Gracia, Z.J. Xu, Spin-related electron transfer and orbital interactions in oxygen electrocatalysis, *Adv. Mater.* 32 (2020), 2003297.